Advances in Geo-Energy Research

Vol. 10, No. 2, p. 117-132, 2023

Original article

Numerical modeling of micro-particle migration in channels

Dongying Wang[1,2,3]*, Qin Qian[1], Anhai Zhong[1], Mingjing Lu[1,2], Zilin Zhang[1]

[1]*Petroleum Engineering Technology Research Institute of Shengli Oilfield, Sinopec, Dongying 257000, P. R. China*

[2]*Postdoctoral Scientific Research Working Station of Shengli Oilfield, Sinopec, Dongying 257000, P. R. China*

[3]*College of Petroleum of Engineering, China University of Petroleum, Beijing 102249, P. R. China*

Keywords:
Micro-particle migration
channel
particle agglomerate
lattice Boltzmann method
discrete element method
immersed moving boundary scheme

Cited as:
Wang, D., Qian, Q., Zhong, A., Lu, M., Zhang, Z. Numerical modeling of micro-particle migration in channels. Advances in Geo-Energy Research, 2023, 10(2): 117-132.
https://doi.org/10.46690/ager.2023.11.06

Abstract:
Physicochemical forces exert non-neligible effects on the migration of micro-particles in channels. Experiments, analytical and non-resolved computational fluid dynamics models have failed to decipher the dynamic behaviors of these particles when carried by fluid flow. In this paper, particle-scale numerical simulation is conducted to study the adhesive micro-particle migration process during duct flow in channels with a large characteristic dimension ratio and those with relatively small such ratio based on the coupled lattice Boltzmann method-discrete element method. The interaction between particle and fluid flow is dealt with by the immersed moving boundary condition. For micro-particle migration in duct flow, the effects of hydrodynamic force, adhesive force and particle concentration on the aggregation of particles are investigated. Based on the concept of hydrodynamic and adhesive force ratio, a stable aggregation distribution map is proposed to help analyze the distribution and size of the formed agglomerates. For micro-particle migration in channels with small characteristic dimension ratio, the general particle migration process is analyzed, which includes single particle retention, followed by particle capture, and the migration of large agglomerates. It is concluded that two factors accelerate single particle retention in a curved channel. Moreover, it is established that higher fluid flow rate facilitates the formation of large and compact agglomerate, and blockage by this can cause severe damage to the conductivity of the channel.

1. Introduction

Micro-particle migration and aggregation in fluid flow in channels are ubiquitous processes in nature and engineering practice. This is beneficial to some fields, such as the flocculation and settling of fine sediment during wastewater treatment and spherical crystallization in pharmaceutical processes. However, in other fields, the aggregation and deposition of fine particles will lead to severe problems, especially in oil & gas exploration. For example, the agglomeration of coal fines formed during coal-bed methane (CBM) production will enhance the possibility of blocking of coal cleat and propped fracture, which can lead to severe damage to coal permeability (Zou et al., 2014; Wang et al., 2022, 2023). The aggregation of fine particles is affected by the combined action of various physical and physicochemical forces. The London/Van der Waals force resulting from the interaction of dipoles between two any approaching materials is one of the main physicochemical forces and is generally an attractive force between particles or between particle and plane (Hamaker, 1937). Although this is a weak interaction force, when the particle diameter decreases to less than 100 micrometers, it becomes the dominant factor influencing the dynamic characteristics of particles by promoting their aggregation. The flocculation of fine sediment in a colloid system is the macroscopic result of this attractive interaction. Besides the physicochemical force, in fluid flow, the main physical force is the hydrodynamic force. Intense hydrodynamic force can increase the collision frequency of particles, while it is more likely to tear the agglomerate apart. Therefore, the size of particle aggregations is the joint effect of attractive forces and hydrodynamic forces.

In porous media, the solute transport mass balance equation is commonly used in deep bed filtration (DBF) theory to char-

Yandy Scientific Press

*Corresponding author.
E-mail address: t-wangdongying.slyt@sinopec.com (D. Wang); qianqin.slyt@sinopec.com (Q. Qian); zhonganhai.slyt@sinopec.com (A. Zhong); lumingjing001@126.com (M. Lu); zhangzilin.slyt@sinopec.com (Z. Zhang).

Received September 14, 2023; revised October 2, 2023; accepted October 26, 2023; available online October 30, 2023.

acterize colloidal transport (Bradford et al., 2003; Rousseau et al., 2008; Zamani and Maini, 2009). This theory suggests that fine particles are prone to deposition and adhesion to the walls, leading to potential entrapment. Based on the capillary tube bundle model and the Carman-Kozeny equation, Hu et al. (2021) studied the permeability evolution model of propped fracture considering coal powder migration and deposition. A new DBF network model consisting of the particle mass balance equation and particle trajectory model was proposed to evaluate the particle invasion characteristic within the propped fracture (Qi et al., 2023). Although the filtration theory has been frequently employed in lab- and field-scale studies, it is important to note that its filtration coefficients are typically derived from core tests and the findings are expressed as macroscopic averages, which causes the loss of information on the dynamic behaviors of a single particle. Besides, this theory cannot describe the evolution of the characteristic particle size with the aggregation of particles under the effects of adhesive force.

Based on the discrete element method (DEM), the modeling of micro-particle dynamic behaviors at the particle-scale can help us investigate the effects of hydrodynamic force, adhesive force, inertia force, and collision on the structure and size of agglomeration (Chen et al., 2019, 2020). Based on computational fluid dynamics (CFD)-DEM considering cohesive contact, Shao et al. (2021) revealed the clogging mechanisms of micro-channels caused by fine wet particles. They used the Stokes number that represents the collision frequency of particles and the inverse of Weber number that describes the cohesive action to analyze the clogging-nonclogging transition. In the CFD-DEM method, the fluid flow is generally described by solving the Navier-Stokes equations, the particle migration is described by Newton's second law, and the fluid-solid coupling is represented by the interaction force (moment) between the fluid and the particle (Tsuji et al., 1993; Wu and Guo, 2012; Norouzi et al., 2016). In practical engineering, the non-resolved CFD-DEM method is usually used to deal with the problem of immersed particle migration in view of the computational efficiency. In this kind of method, a fluid cell can accommodate multiple particles, and the fluid forces are calculated by the local averaged method that is related to the local porosity of the cell. Therefore, it cannot describe the particle flow at the scale of a single particle (Yang et al., 2020).

The coupled lattice Boltzmann method (LBM)-DEM is an alternative way to resolve the fluid-solid interaction. The core of LBM focuses on the description of probability distribution function within the nodes themselves, which makes implementation simple without discretizing the non-linear advection term as that in the conventional CFD equations. Besides, LBM is well applicable to the laminar flow in channels with complex geometric shapes such as porous media. Coupled with LBM and DEM, it can precisely resolve the interactions between particles and between particle and fluid, which can help us to replicate the detailed dynamic behaviors of moving particles. For boundaries with complex geometries that fail to conform with the Cartesian lattice system, such as porous media and moving particles, there are mainly three types of boundary conditions in LBM-DEM: modified bounce back (MBB) method (Ladd, 1994a, 1994b), immersed boundary method (IBM) (Peskin, 1972; Feng and Michaelides, 2004) and immersed moving boundary (IMB) (Noble and Torczynski, 1998; Cook, 2001, 2004; Wang et al., 2020). In the MBB method, the real solid geometries are simplified to staircase shapes, followed by the application of the bounce back method. However, as the particles move, the staircase shape will change, leading to discontinuous hydrodynamic force and torque. Wang et al. (2019) compared the IBM and IMB scheme by conducting single particle sedimentation in viscous fluid, and found that the fluid force calculated by the IMB scheme develops smoothly, while the drag forces calculated by the IBM fluctuate significantly. Compared with the MBB and IBM schemes, the IMB scheme is more efficient and stable. The LBM-IMB-DEM has been constantly improved and widely employed in many particle migration problems. Yang et al. (2019) presented a series of benchmark cases to validate the numerical accuracy, stability and efficiency of the LBM-IMB-DEM algorithm. Liu and Wu (2019) and Wang et al. (2020) proposed the modified weighting function to deal with the situation where a lattice is covered by two or more solid particles. Some practical applications with the LBM-IMB-DEM scheme, such as the initiation and propagation of hydraulic fracture (Wang et al., 2017), performance of granular filters (Wang et al., 2018), migration and agglomeration of adhesive micro-particle suspensions (Liu and Wu, 2020), transport of particles suspended within a temperature-dependent viscosity fluid (McCullough et al., 2020), and submarine landslides (Yang et al., 2020), have been presented, which demonstrates that the coupled LBM-DEM with the IMB scheme is a promising method.

In LBM-DEM, the fluid domain is finely divided into regular lattices that have smaller sizes than that of particles, and it can provide extensive pore-scale information. This is helpful to find some potential migration mechanisms, while other models, such as the DBF theory, non-resolved CFD model, and experimental studies fail to accomplish this task. However, limited by the large memory demand of LBM, its restriction for weakly compressible flow, and the much smaller DEM time step, LBM-DEM is not easy to be upscaled to the core and field scales. Indirect application can be achieved by improving the analytical model that can be directly applied to the real reservoir. For example, the DBF theory is based on the relatively simple porous media model (such as tube bundle model (Bedrikovetsky et al., 2011; Hu et al., 2021) and unit element (Qi et al., 2023)). A thorough understanding of the dynamic behavior of particles in the channels (if regarded as the simple porous media model or the unit element in DBF theory), such as blockage, bridging, sorption, sedimentation, and aggregation, may be helpful to improve the model of DBF theory. Moreover, the aggregation of micro-particles will make the characteristic size of moving particles generally larger than that of a single particle. Besides the drag force and Van der Waals force considered in the particle trajectory in the DBF network model, the lift force and lubrication force also have important influences on the migration of micro-particles (Chun and Ladd, 2006; Choi et al., 2010). Therefore, through current LBM-DEM modeling, specifying the characteristic

size of agglomerates and their distribution might be helpful to improve the DBF network model. In further research, with the improvement of the model and combined with the digital core, particle migration in more complicate porous media can be conducted to help determine the empirical coefficients in the DBF theory.

The aggregation and retention of micro-particles in the channel are closely related to hydrodynamic force, adhesive force and the channel geometry, with these factors significantly affecting the particle size and distribution in the channel. In this paper, particle-scale numerical modeling of micro-particle migration in duct flow and curved channel flow are conducted, in which the fluid flow is described using LBM, while the DEM with Johnson-Kendall-Roberts (JKR) theory is applied to resolve the interactions between adhesive particles. The IMB considering the partially saturated computational cells based on the local solid fraction is utilized to deal with the interactions between fluid flow and solid particles. The characteristic dimension ratio (R_d) is proposed to represent the particle diameter relative to the size of the channel. Changes in the size and distribution of stable agglomerates in duct flow with a large R_d with variations in the pressure gradient, surface energy and particle concentration are investigated. Based on the concept of hydrodynamic and adhesive force ratio (R_F), a stable aggregation distribution map is proposed and validated to help analyze the distribution and size of the formed agglomerate in duct flow. For the migration of micro-particles in channels with a relatively small R_d, based on the numerical results, the general particle migration process and the two factors that accelerate the single particle retention in curved channels are concluded. Moreover, the mechanism of higher fluid flow rate leading to more severe permeability damage is investigated, though larger hydrodynamic forces facilitate the migration of particles in the channel.

2. Numerical model

2.1 Lattice Boltzmann method

LBM is a promising fluid solver that evolved from the lattice gas model in the late 1980s (McNamara and Zanetti, 1988; Wolf-Gladrow, 2004). The lattice Boltzmann equation (LBE) with Bhatnagar-Gross-Krook (BGK) approximation (Qian et al., 1992; Shan and Chen, 1993; Guo et al., 2002), shown in Eq. (1), is a discrete type of continuous Boltzmann equation:

$$\begin{aligned} &f_i(\mathbf{x}+\mathbf{c}_i\triangle t, t+\triangle t)-f_i(\mathbf{x},t) \\ &=-\frac{\triangle t}{\tau}\left[f_i(\mathbf{x},t)-f_i^{eq}(\mathbf{x},t)\right]+S_i(\mathbf{x},t) \end{aligned} \tag{1}$$

$$\tau = 0.5+\frac{v}{c_s^2\triangle t} \tag{2}$$

$$f_i^{eq}(\mathbf{x},t)=w_i\rho\left[1+\frac{\mathbf{u}\cdot\mathbf{c}_i}{c_s^2}+\frac{(\mathbf{u}\cdot\mathbf{c}_i)^2}{2c_s^4}-\frac{(\mathbf{u}\cdot\mathbf{u})^2}{2c_s^2}\right] \tag{3}$$

where $f_i(\mathbf{x},t)$ represents probability distribution function in the i_{th} direction, dimensionless; $f_i^{eq}(\mathbf{x},t)$ represents equilibrium distribution function in the i_{th} direction, dimensionless; $\triangle t$ represents LBM time step, dimensionless; τ represents relaxation time, dimensionless; $S_i(\mathbf{x},t)$ represents the source term of external force on the fluid phase in the i_{th} direction, dimensionless; ρ represents fluid density, kg/m^3; $\mathbf{c}_i$ represents particle discrete velocity in the i_{th} direction, dimensionless; c_s represents lattice speed of sound, dimensionless; v represents fluid kinematic viscosity, m^2/s; w_i represents weight in the i_{th} direction, dimensionless; $\mathbf{u}$ represents fluid velocity, m/s.

LBE is generally obtained by discretizing the continuous Boltzmann equation in velocity space using series expansion by Hermite polynomials and in time-physical space using the method of characteristics (Krüger, 2007). It describes the process of collision, and the streaming of particles that are included in an imaginary particle package at the lattice node. The collision is completely local while the streaming is linear, and this makes LBM easy to implement and parallelize. It should be noted that lattice units are used and the variables are defined to be dimensionless, although they are actually not.

Guo's force scheme (Guo et al., 2002) is used in this paper:

$$S_i(\mathbf{x},t)=\left(1-\frac{\triangle t}{2\tau}\right)\omega_i\left[\frac{c_{i\alpha}}{c_s^2}+\frac{(c_{i\alpha}c_{i\beta}-c_s^2\delta_{\alpha\beta})u_\beta}{c_s^4}\right]F_\alpha \tag{4}$$

where $\delta_{\alpha\beta}$ represents the Kronecker symbol, dimensionless; α and β represent the component number of a vector, dimensionless; $c_{i\alpha}$ and $c_{i\beta}$ represent α_{th} and β_{th} components of $\mathbf{c}_i$, respectively; F_α represents the α_{th} compnent of external force density $\mathbf{F}$, kg/(m$^2\cdot$s^2); u_β is the β_{th} components of $\mathbf{u}$, m/s.

The macroscopic fluid properties, such as density and velocity, can be obtained by the weighted sum of the velocity moments of $f_i(\mathbf{x},t)$:

$$\rho(\mathbf{x},t)=\sum_i f_i(\mathbf{x},t) \tag{5}$$

$$\rho(\mathbf{x},t)\mathbf{u}(\mathbf{x},t)=\sum_i f_i(\mathbf{x},t)\mathbf{c}_i+\frac{\mathbf{F}\triangle t}{2\rho(\mathbf{x},t)} \tag{6}$$

where $\rho(\mathbf{x},t)$ represents fluid density, kg/m^3.

In this paper, the D3Q19 model shown in Fig. S1 is adopted, where D is the number of spatial dimensions and Q is the number of velocities in the set. The velocity sets and the corresponding weights are:

$$\begin{aligned} [\mathbf{c}_i, i=0,\cdots,18] &= c\mathbf{e}_i \\ &= c\begin{bmatrix} 0 & 1 & -1 & 0 & 0 & 0 & 0 & 1 & -1 & 1 \\ 0 & 0 & 0 & 1 & -1 & 0 & 0 & 1 & -1 & -1 \\ 0 & 0 & 0 & 0 & 0 & 1 & -1 & 0 & 0 & 0 \\ -1 & 1 & -1 & -1 & 1 & 0 & 0 & 0 & 0 & \\ 1 & 0 & 0 & 0 & 0 & 1 & -1 & 1 & -1 & \\ 0 & 1 & -1 & 1 & -1 & 1 & -1 & -1 & 1 & \end{bmatrix} \end{aligned} \tag{7}$$

where c is a coefficient, dimensionless; $\mathbf{e}_i$ represents the spatial directions of velocity set, dimensionless.

$$w_i(i=0,\cdots,18)=\begin{cases} 1/3 & i=0 \\ 1/18 & i=1,\cdots,6 \\ 1/36 & i=7,\cdots,18 \end{cases} \tag{8}$$

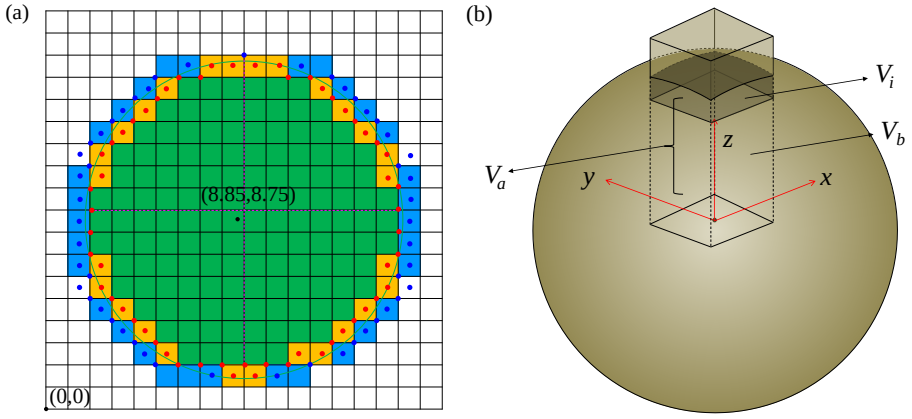

Fig. 1. The four types of cells (a) and the specific intersection configuration of sphere and cube (b).

2.2 Immersed moving boundary scheme

There is momentum exchange between moving particles and fluid. Noble and Torczynski (1998) proposed the IMB scheme by introducing an additional collision term Ω_i^s and weighting function (B) to deal with problems where the computational cells are partially saturates by solids. Liu and Wu (2019) and Wang et al. (2020) modified the weighting function to make the IMB appropriate for situations where a cell is covered by more than one particle. The corresponding lattice Boltzmann equations are therefore revised as:

$$\begin{aligned} &f_i(\mathbf{x}+\mathbf{c}_i\triangle t, t+\triangle t)-f_i(\mathbf{x},t)= \\ &-(1-B)\frac{\triangle t}{\tau}\left[f_i(\mathbf{x},t)-f_i^{eq}(\mathbf{x},t)\right]+\sum_p(B_p\Omega_i^s) \\ &+(1-B)S_i(\mathbf{x},t)\triangle t \end{aligned} \tag{9}$$

$$B_p=\frac{\varepsilon_p(\tau-0.5)}{(1-\varepsilon_t)+(\tau-0.5)} \tag{10}$$

$$\Omega_i^s=f_{-i}(\mathbf{x},t)-f_{-i}^{eq}(\rho,\mathbf{u})+f_i^{eq}(\rho,\mathbf{u}_s^m)-f_i(\mathbf{x},t) \tag{11}$$

where ε_p represents the solid fraction of one of the solid particles covering the cell, dimensionless; $\varepsilon_t=\sum_p\varepsilon_p$ represents the total solid fraction of one cell, dimensionless; B_p represents the contribution to the weighting function from one of the particles covering the cell, dimensionless; $B=\sum_p B_p$ represents total weighting function, dimensionless; Ω_i^s represents additional collision operator in the i_{th} direction under the effects of solid particles, dimensionless; $f_{-i}^{eq}(\rho,\mathbf{u})$ and $f_i^{eq}(\rho,\mathbf{u}_s^m)$ respectively represent probability distribution function and equilibrium distribution function in the reverse i_{th} direction, dimensionless; $\mathbf{u}_s^m$ is the mean velocity of solid particles covering one cell, m/s.

The hydrodynamic force $\mathbf{F}_k^f$ on the k_{th} particle can be obtained by summing all the momenta transfer along all velocity directions at all lattice cells covered by the solid particle:

$$\mathbf{F}_k^f=-\sum_j B_j\left(\sum_j\Omega_i^s\mathbf{e}_i\right) \tag{12}$$

$$\mathbf{M}_k^f=-\sum_j\left[(\mathbf{x}_j-\mathbf{x}_k)B_j\left(\sum_j\Omega_i^s\mathbf{e}_i\right)\right] \tag{13}$$

where j represents the identifier of serial number of cells covered by the same solid particle, dimensionless; B_j represents the contribution of weighting function in the j_{th} covered cell, dimensionless; $\mathbf{M}_k^f$ represents the hydrodynamic torque on solid particle k, N·m; $\mathbf{x}_j$ represents the center of the j_{th} covered cell by the solid particle, m; $\mathbf{x}_k$ represents the centroid of solid particle k, m.

The calculations of fluid force and torque exerted on the particle are closely related to the weighting function that is linked to the solid fraction of a cell (Eqs. (12)-(13)). Therefore, the solid fraction should be accurately identified for all cells at each time step. However, with the increasing number of particles and particle size, the computational cost will be greatly increased. Two kinds of measures can be taken to resolve this problem. The first is to identify the cells covered by the solid particle in advance, and the second is to efficiently calculate the intersection volume of sphere and cube. The cells are classified into four types (Liu and Wu, 2020; Wang et al., 2020). The green, yellow, blue, and white filled cells in Fig. 1 are solid cells, solid boundary cells, fluid boundary cells, and fluid cells in a two dimensional situation, respectively. Obviously, the solid fractions of fluid and solid cells are 1 and 0, respectively. For fluid boundary cells and solid boundary cells, an efficient boundary cell tracing method called layer-by-layer tracing method is used, which is both applicable to two dimensional and three dimensional situations proposed in our previous research (Wang et al., 2022).

Jones and Williams (2017) summarized the currently applied methods for calculating the sphere-cube intersection volume, such as Monte-Carlo sampling, sub-division sampling, edge-intersection averaging, and polyhedral convex hull. After comparing these methods, they proposed one fast computation method called linear approximation. This method is a specific analytical solution when the grid element orientation with respect to the particle surface is shown in Fig. 1(b), and the solid fraction is linearly calculated as:

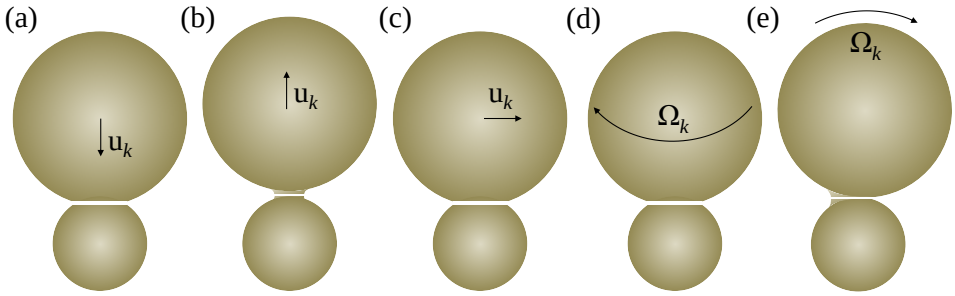

Fig. 2. Interactions between two adhesive particles: (a) Normal impact, (b) necking in normal extension, (c) shearing, (d) twisting and (e) rolling.

$$\varepsilon_p = -L + V_a - r + 0.5 \tag{14}$$

where L represents the distance from the cell center to the particle surface, m; V_a represents the summation of intersection volume V_i and the volume of the cube between the lower cell face and the particle center V_b, which can be obtained by integration based on the spherical equation, m^3; r is the radius of the particle, m.

2.3 Discrete-element method

In DEM, the linear and angular velocities can be updated using Newton's second law, as shown in Eqs. (15)-(16), and the particle interaction models are mostly based on the Hertz model (Hertz, 1882) or the JKR theory extended by Johnson et al. (1971) when the Van der Waals adhesion is considered. In this study, the forces exerting on the particles include hydrodynamic forces that are obtained by the IMB scheme, gravity, and contact forces. For the contacted forces of adhesive particles, besides the elastic forces and the damping forces, the Van der Waals adhesive force and the resultant resistances are also taken into account (Marshall, 2009) (Fig. 2):

$$m_k \frac{\mathrm{d}\mathbf{u}_k}{\mathrm{d}t} = \mathbf{F}_k^c + \mathbf{F}_k^f + (\rho_k - \rho) V_k \mathbf{g} \tag{15}$$

$$\mathbf{I}_k \frac{\mathrm{d}\Omega_k}{\mathrm{d}t} = \mathbf{M}_k^c + \mathbf{M}_k^f \tag{16}$$

where m_k represents the mass of solid particle k, kg; $\mathbf{u}_k$ represents transitional velocity of solid particle k, m/s; $\mathbf{F}_k^c$ represents the total contact forces of solid particle k exerted by other particles and walls on it, N; ρ_k represents solid particle density, kg/m^3; V_k represents the volume of solid particle k, m^3; $\mathbf{I}_k$ represents the inertia tensor of solid particle k, $kg{\cdot}m^2$; Ω_k represents the local rotational velocity of solid particle k, rad/s; $\mathbf{M}_k^c$ represents the sum of the contact torques on solid particle k, N·m; $\mathbf{g}$ represents the acceleration of gravity, m/s^2.

The contact force $\mathbf{F}^c$ and torque $\mathbf{M}^c$ between two colliding particles are expressed as (Marshall, 2009):

$$\mathbf{F}^c = F_n \mathbf{n} + F_s \mathbf{t}_s \tag{17}$$

$$\mathbf{M}^c = r F_s (\mathbf{n} \times \mathbf{t}_s) + M_r (\mathbf{t}_r \times \mathbf{n}) + M_t \mathbf{n} \tag{18}$$

where F_n represents normal force, N; F_s represents tangential force due to the sliding friction, N; M_r represents rolling resistance, N·m; M_t represents twisting resistance, N·m; $\mathbf{n}$, $\mathbf{t}_s$ and $\mathbf{t}_r$ are respectively the normal, tangential, and rolling direction unit vectors, dimensionless.

The magnitude of normal forces for non-adhesive F_n^n and that for adhesive particles F_n^a are given as (Liu and Wu, 2020):

$$F_n^n = -F_n^e - F_n^d = -k_n \delta_n - \eta_n \mathbf{u}_R \mathbf{n} \tag{19}$$

$$F_n^a = -F_n^e - F_n^d = -4F_C \left[(a/a_0)^3 - (a/a_0)^{3/2} \right] - \eta_n \mathbf{u}_R \mathbf{n} \tag{20}$$

where F_n^e and F_n^d respectively represent the magnitude of normal elastic force and damping force, N; k_n represents elastic stiffness, N/m; $F_C = 3\pi\gamma R$ represents critical force, N; R represents effective particle radius, m; γ represents surface energy, J/m^2; δ_n represents normal overlap, m; a represents contact region radius, m; a_0 represents equilibrium contact region radius, m; η_n represents normal dissipation coefficient, kg/s; u_R represents relative velocity at the contact point, m/s.

The variations in the normal elastic force with the change of overlap of normal particles are not the same for the non-adhesive particles and adhesive particles (Fig. S2, in which the particle diameter, elastic modulus and surface energy are 5 μm, 0.99 GPa and 3 mJ/m^2, respectively). For non-adhesive particles, when δ_n is 0, then F_n^e is also equal to 0. However, for adhesive particles, even when δ_n is negative, as presented in Fig. 2(b), there is still a tensile force. The maximum tensile force is the critical force F_C that is positively related to the surface energy.

The sliding, rolling and twisting resistances are given as:

$$F_s = -\min\left[k_t \xi_t \mathbf{t}_s + \eta_t \mathbf{u}_R \mathbf{t}_s, F_s^c\right] \tag{21}$$

$$M_t = -\min\left[k_q \xi_q + \eta_q \omega_t, M_t^c\right] \tag{22}$$

$$M_r = -\min\left[k_r \xi_r \mathbf{t}_r + \eta_r \mathbf{u}_l \mathbf{t}_r, M_r^c\right] \tag{23}$$

where k_t represents sliding stiffness, N/m; k_q represents twisting stiffness, N·m; k_r represents rolling stiffness, N; ξ_t represents sliding displacement, m; ξ_q represents twisting displacement, rad; ξ_r represents rolling displacement, m; η_t represents tangential dissipation coefficient, kg/s; η_q represents torsional friction coefficients, N·m·s; η_r represents rolling friction coefficients, N·s; $\mathbf{u}_l$ represents rolling velocity, m/s;

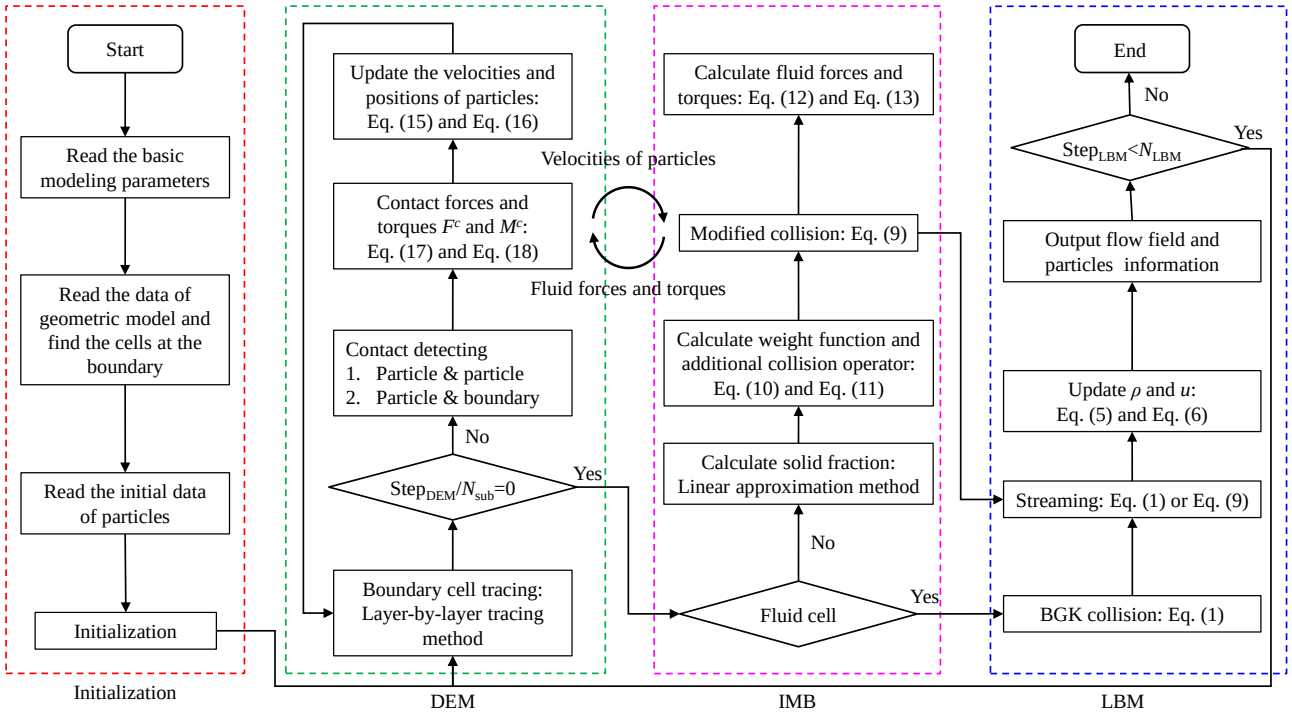

Fig. 3. Flowchart of the LBM-IMB-DEM scheme.

F_s^c, M_t^c, and M_r^c represent the corresponding critical resistance values; ω_t represents relative twisting rate, rad/s.

The coefficients and the corresponding expressions in Eqs. (17)-(23) are concluded in Table S1 of the Supplementary material.

2.4 Implementation of LBM-IMB-DEM

The interaction between the fluid and solid particles is achieved by the IMB scheme that is still in the frame of LBM. The implementation of LBM-IMB-DEM is achieved by an in-house C++ code and includes an initialization module and solving modules (Fig. 3). In the initialization module, information about the fluid field (fluid density, viscosity, pressure gradient, etc.), DEM parameters (stiffness, restitution coefficient, surface energy, etc.), and evolution parameters, are firstly read, and then the fluid field is initialized. When it comes to the solving modules, in each DEM sub-cycle, the boundary cells of particles are traced using the layer-by-layer tracing method mentioned in section 2.2. Based on the tracing results, the contacts between particles and those between particle and wall are determined. After introducing the contact forces (Eqs. (17)-(18)) and the hydrodynamic forces (Eqs. (12)-(13)) into Newton's second law (Eqs. (15)-(16)), the velocity and position of particles can be updated. In the IMB module, based on the tracing results of the layer-by-layer tracing method, the solid fractions of fluid boundary cells and solid boundary cells are calculated by the linear approximation method (Eq. (14)), and that of solid cells is set to be 1.0. For cells partially or fully covered by particles, the weighting function B_p (Eq. (10)) and additional collision term Ω_i^s (Eq. (11)) are introduced to Eq. (9) to reflect the effects of particles on the fluid flow. For cells not covered by particles, the original LBE Eq. (1) is applied to obtain the fluid field. The LBM module includes BGK collision for fluid cells, streaming, and moment update, which are the general processes of LBM calculation.

3. Model validation

Numerical simulations of the duct flow with different $\triangle x$ are conducted to verify the numerical accuracy of LBM, the single particle sedimentation in viscous fluid to validate the interaction between flow and particle, and the two-particle Drafting-Kissing-Tumbling (DKT) simulation to reflect the interaction between particles.

As described in section 2.1, lattice units are used in LBM calculation. The lattice constant $\triangle x$, the time step $\triangle t$ and the average density ρ_0 are generally set as the basic reference variables. Firstly, according to the size of fluid flow space and the possible maximum velocity in the flow field, the values of $\triangle x$ and $\triangle t$ are determined to make the total number of cells not too large and the dimensionless maximum velocity in the flow field much less than c_s. Then the relaxation time τ calculated by Eq. (2) is checked to be larger than 0.5 and not much larger than 1. For example, in a 58 × 58 × 200 flow space, with $\triangle x = 1$ μm, $\triangle t = 5 \times 10^{-8}$ s and $\rho_0 = 1{,}000$ kg/m^3, and the maximum number of cells is 672,800, the maximum dimensionless velocity u^* in the fluid flow field with a 4.0 m/s maximum physical fluid flow velocity is 0.2, and the τ is 0.65. Once the basic reference values have been obtained, the other variables can be non-dimensionalized through dimension analysis. For example, the dimension of Youngs modulus is Pa (kg/m/s^2), and its lattice value can be obtained by multiplying

Table 1. The parameters used in LBM modeling duct flow with different $\triangle x$ values.

Parameter	Physical value	Lattice value
Lattice constant	1, 2 μm	1
Fluid density	1,000 kg/m^3	1
Fluid kinetic viscosity	1×10^{-6} m^2/s	0.05
Time step	5×10^{-8}, 2×10^{-7} s	1
Relaxation time	/	0.65
Channel size	100 × 30 × 30 μm	100 × 30 × 30, 50 × 15 × 15

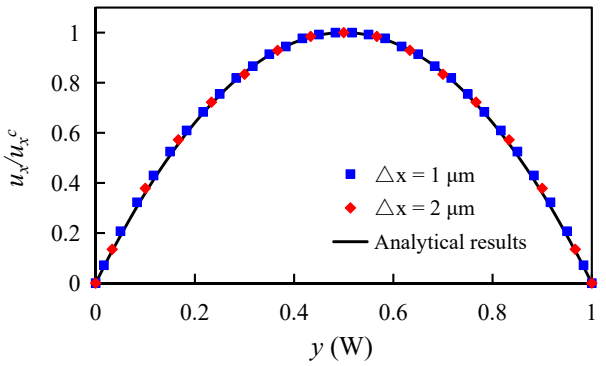

Fig. 4. Velocity profile in duct flow with different lattice constants.

it with the coefficient $\triangle t^2/\rho_0/\triangle x^2$, which is equal to 2,475.

3.1 Duct flow

Numerical simulations of duct flow with different $\triangle x$ are conducted to verify the numerical accuracy of LBM, and the parameters are shown in Table 1. The lattice constant and time step are adjusted to make the relaxation time constant.

The x-velocity distribution in duct flow can be analytically calculated by (Liu and Wu, 2019):

$$u_x(y,z) = \frac{1}{2\mu}\frac{\partial p}{\partial x}y(L_h - y) - \frac{4L_h^2}{\mu\pi^3}\frac{\partial p}{\partial x}\sum_{m=1}^{\infty}\frac{\sin(\beta_m y)}{(2m-1)^3}\frac{\sinh(\beta_m z)+\sinh[\beta_m(L_w - z)]}{\sinh(\beta_m L_w)} \quad (24)$$

where μ represents fluid dynamic viscosity, Pa·s; p represents pressure, Pa; y and z respectively represent the position coordinates in the flow field in y and z directions; L_h and L_w respectively represent the height and width of the channel, m; $\beta = (2m-1)\pi/L_h$.

The velocity profile in duct flow along the y direction in the z plane passing through the central line has a parabolic shape (Fig. 4, in which y is the y-coordinate, m; W is the width of the channel, m). It can be found that the numerical results both with 1 and 2 μm lattice constant agree well with the analytical results. From the point of fluid flow modeling efficiency, a large lattice constant should be applied. However, in this study, the particle size is 5 μm, and a 2 μm lattice constant will decrease the resolution of the particle, which can affect the accuracy of interaction between the fluid and particles. Therefore, in this study, the lattice constant is determined to be 1 μm.

Table 2. Parameters for single particle sedimentation in viscous fluid.

Parameter	Physical value	Lattice value
Lattice constant	5×10^{-5} m	1
LBM time step	4.167×10^{-5} s	1
Fluid density	1,000 kg/m^3	1
Fluid kinetic viscosity	0.25, 0.5, 1, 2 $\times 10^{-6}$ m^2/s	0.004167, 0.008334, 0.016668, 0.033336
Relaxation time	/	0.5125, 0.525, 0.55, 0.6
Particle diameter	2.5×10^{-4} m	5
Particle density	2,000 kg/m^3	2
DEM time step	4.167×10^{-7} s	0.01
Size of flow space	2.5 × 2.5 × 6 mm	50 × 50 × 120

3.2 Single particle sedimentation in viscous fluid

Single particle sedimentation is a common case that can be applied to validate the coupled LBM-DEM scheme. The simulation parameters are shown in Table 2.

After the velocity of particle settling has stabilized, the drag coefficient C_D can be calculated by the following equation:

$$C_D = \frac{2F_D}{\pi\rho r^2 u_t^2} \quad (25)$$

where F_D represents the magnitude of drag force, N; u_t represents the settling velocity of particle, m/s.

The expression of drag coefficient for a settling sphere particle is expressed by (Abraham, 1970):

$$C_D = C_0\left(1 + \frac{\delta_0}{\sqrt{\mathrm{Re_p}}}\right)^2 \quad (26)$$

where δ_0 represents a parameter for drag coefficient and is equal to 9.06, dimensionless; C_0 represents a parameter for drag coefficient and $C_0\delta_0^2$ = 24, dimensionless; $\mathrm{Re_p}$ denotes particle Reynolds number, dimensionless.

The simulated drag coefficient and the one calculated by Eq. (26) are compared, and the result is presented in Fig. 5. It can be found that the numerically obtained and correlation calculated drag coefficients agree well when the $\mathrm{Re_p}$ is relatively low, while the error appears when the $\mathrm{Re_p}$ is high.

3.3 Two-particle DKT simulation

When two particles placed at a limited distance in the vertical direction are settling under the effects of gravity, some

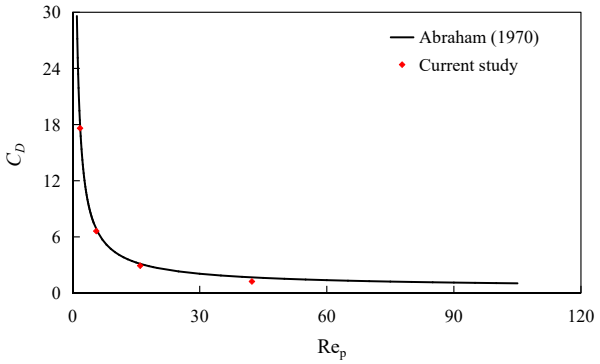

Fig. 5. Drag coefficient for a settling particle in viscous fluid.

direct interactions or indirect ones delivered by the fluid may occur, called the DKT phenomenon. DKT is generally used to validate the coupled LBM-DEM scheme (Strack and Cook, 2007; Wang et al., 2020; Chen et al., 2021). In this simulation, particle 1 is statically placed at (50.025, 10, 390) and particle 2 is statically place at (49.975, 10, 377.5). The small position deviation of both particles from the center line in the x direction is set to break the strong symmetry of the flow field (Tao et al., 2018; Chen et al., 2021). For the DKT simulation of adhesive particles, the surface tensions between the particles and those between the particle and wall are set to be 3 mJ/m^2. The simulation parameters are shown in Table 3.

The trajectories of the pair of particles both considering non-adhesive and adhesive effects are shown in Fig. S3(a). During the short period of time after being released, as shown by Figs. S3(b)-S3(d), the two particles have almost the same velocity evolution process. However, when the catching particle (particle 1) is affected by the local low pressure area caused by the trailing vortex of the leading particle (particle 2), it has a higher accelerated velocity than the leading particle as a result of low flow resistance, and it starts to catch up with the leading particle, defined as the drafting process. There is no difference between non-adhesive and adhesive particles during this process, because in JKR theory, the adhesive force is assumed to only work in the contact area. For non-adhesive particles, after the catching particle kisses the leading one, the temporary elongated body formed by the two particles could be affected by the small perturbations from the ambient flow field, that would push the leading particle to the left and make the catching one tumble to the right. During the tumbling process, the leading particle continually exerts a $y+$ moment of force on the leading one, which leads to an increasing y rotation velocity of two particles in opposite directions, as shown in Fig. S3(d). When these two particles are separated by the fluid forces, their y rotation velocities gradually decrease as a result of hydrodynamic resistance and eventually to 0 when they collide with the bottom wall.

For adhesive particles, after the pair of particles have collided with each other, they form a more stable elongated body bonded by the strong adhesive force. The hydrodynamic forces fail to push them apart and they settle as an agglomerate and rotate together. The vertical settling velocity of the agglomerate is larger than that of a single particle, which can be explained by that the bonded particle pair has lower rotation speed compared with that of the non-adhesive particle, as shown by Fig. S3(d). The rotation motion reduces the particle velocity (Chen et al., 2021). In general, the variation trend of the particles agrees well with that in the literature (Strack and Cook, 2007).

Table 3. Parameters for DKT simulation.

Parameter	Physical value	Lattice value
Lattice constant	1×10^{-4} m	1
LBM time step	5×10^{-4} s	1
Fluid density	1,000 kg/m^3	1
Fluid kinetic viscosity	1×10^{-6} m^2/s	0.05
Relaxation time	/	0.65
Particle diameter	1 mm	10
Particle density	1,020 kg/m^3	1.02
DEM time step	5×10^{-6} s	0.01
Size of flow space	10 × 2 × 40 mm	100 × 20 × 400

4. Numerical results and discussion

The characteristic dimension ratio reflects the degree of the particles being affected by the wall. Under a large R_d, the collision frequency between particles and the wall is low. Besides, most of the moving particles away from the wall feel slight effects from boundary. Numerical simulations of particle migration in two kinds of fluid flow are conducted: duct flow with a large R_d and fluid flow with a relatively small one. In the modeling of particle migration in the channel with small R_d, the effect of the wall becomes significant and particle migration in different channel shapes is investigated. The periodic boundary condition for fluid flow and particle periodic boundary condition for particle migration in the x direction are applied. The simulation is carried out under the background of coal particle migration in cleat during single water phase drainage stage in CBM production. In the CBM reservoir, the aperture of the coal cleat falls in between 0.1 and 100 μm (Close, 1993), while the size of produced coal particles ranges from 1-1,000 μm (Zhao et al., 2016), which include large coal particles from hydraulic fractures. Therefore, the physical properties of water and coal are applied as those of the fluid and solid particles, and the coal cleat is regarded as the geometric model. The density of coal is between 1,250 and 1,700 kg/m^3 (Berkowitz, 2012). The Young's modulus of coal ranges from 0.5 to 14 GPa and the Poisson ratio ranges from 0.2 to 0.4. The surface energy of coal calculated based on the adsorption method lies between 0.8574 to 38.39 mJ/m^2 (Wu, 1994). The parameters are finally chosen as shown in Table 4.

4.1 Micro-particle migration in duct flow

During the migration of adhesive particles, the agglomerate size and position are comprehensively affected by a variety of factors, with the three main ones being the fluid flow rate, the

Table 4. General parameters used in the simulation.

Parameter	Physical value	Lattice value
Lattice constant	1 μm	1
Fluid density	1,000 kg/m^3	1
Fluid kinetic viscosity	1×10^{-6} m^2/s	0.05
Time step	5×10^{-8} s	1
Relaxation time	/	0.65
Particle diameter	5 μm	5
Particle density	1,400 kg/m^3	1.4
Time step	5×10^{-10} s	0.01
Youngs modulus	0.99 GPa	2,475
Poisson ratio	0.31	0.31
Friction coefficient	0.3	0.3
Restitution coefficient	0.6	0.6
Critical rolling angle	0.01 rad	0.01 rad

adhesive contacted force, and the particle concentration (C_p). LBM-DEM particle-scale simulations of micro-particle migration in duct flow under different factors are conducted and the flow channel & initial distribution of particles are shown in Fig. 6. The size of the channel is $200 \times 60 \times 60$ μm^3, which is much greater than that of the particle, and the characteristic dimension ratio is 12.

Table 5 Provides the simulation parameters. Cases 1-3 are set to investigate the effects of pressure gradient on the lateral distribution of non-adhesive particles, and cases (4, 6, 9), 5-7, 8-10 are set to study the effects of pressure gradient, particle concentration and surface energy on the aggregation of adhesive particles.

In Poiseuille flow, the dispersed non-adhesive neutrally buoyant particles tend to laterally move to a position at a certain distance away from the central line of the channel. When the Reynolds number (Re) is increased, this phenomenon generally becomes more obvious. Feng et al. (1994) numerically studied the forces affecting the migration of particles and found that the repulsive force resulting from the lubrication effect between the particle and the wall, as well as the lift force that drives the particles close to the wall, lead to this phenomenon. The Re in cases 1-3 is 6.75, 50 and 101, respectively, and the lateral distributions of non-adhesive particles are shown in Fig. 7. Under a low Re, as shown in Fig. 7(a), the particles still evenly disperse in the lateral direction after they have reached a relatively stable state. When the Re is increased to 50, the lateral distribution of these particles presents an annulus pattern and they locate away from the central line of the channel at a distance ranging from $0.3H$-$0.7H$, where H represents half of the side length. When the Re is further increased, the annulus distribution is divided into four parts and the particles start to aggregate close to the four sides of the channel. The lift force in Poiseuille flow is positively dependent on the shear velocity gradient, and under a larger Re, higher lift force can better drive the particles laterally to move them close to the wall. This concentrated distribution enhances the collision frequency, that will also significantly affect the aggregation of adhesive particles.

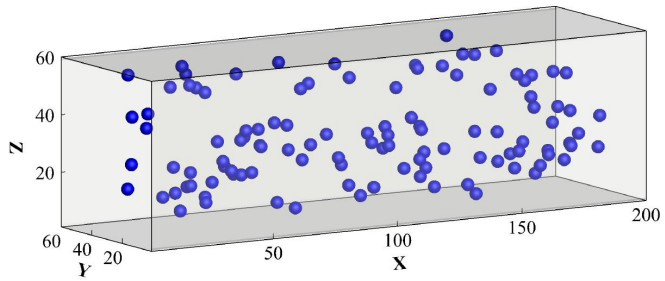

Fig. 6. Geometry of the channel and the initial distribution of particles therein.

With the increase in adhesive contacted force, the size of agglomerates increases while their number decreases (Figs. 8(a)-8(c)). Hydrodynamic force can tear the agglomerate apart, and the larger the aggregation, the harder it is that it will stay intact. Fig. 8(b) and Figs. 8(d)-8(e) show the particle distribution with the increase in Re. At a low Re, more than half of the particles disperse in the form of single particle or small agglomerate composed of a few particles, and some particles are trapped by the wall under the effects of adhesive force. When the Re is increased, as shown in Fig. 8(e), the particles obviously move close to the central line of the channel and some large agglomerates appear. When the Re is further increased, the agglomerates become loose and small agglomerates appear again. The formation of a stable agglomerate has two requirements: the particles are able to collide with each other, and the adhesive force can withstand the disturbance of hydrodynamic force. With the increase in Re, the enhanced lateral movement of particles facilitates their collision; however, a higher hydrodynamic force is unfavorable for the existence of the formed agglomerate. Figs. 8(e)-8(g) depict the variation in particle distribution with the change in C_p. There is no difference in the number of agglomerates, while their size obviously changes. When the C_p is low, the size of the agglomerate is small, while when it is increased to 1%, the agglomerates enlarge evidently. After the C_p is further increased to 1.5%, there is no obvious increase in the characteristic size of the agglomerate.

Based on the above analysis, it is known that the aggregation of adhesive particles is closely related to the hydrodynamic force and adhesive force. The ratio (R_F) shown in Eq. (27) between the two kinds of force is defined to determine whether particles in a specific lateral position of the channel can form a stable agglomerate. For an agglomerate composed of more than two particles, the $\triangle U$ in Eq. (18) is the fluid flow velocity difference between the particle center and the agglomerate center, and the fluid flow velocity is calculated using Poiseuille's law. When $R_F = 1$, the hydrodynamic force and adhesive contacted force are evenly matched. When $R_F < 1$, the adhesive contacted force prevails and the particles in the agglomerate can firmly stick together. With a given surface energy and Re, for each specific center position of agglomerate, there are velocity upper and lower limits within

Table 5. Simulation parameters for micro-particle migration in duct flow.

Case	Pressure gradient (MPa/m)	Surface energy (mJ/m^2)	Particle concentration (%)
1-3	1, 7.4, 15	0	1
4	1	3	1
5-7	5	3	0.5, 1, 1.5
8-10	10	1, 3, 30	1

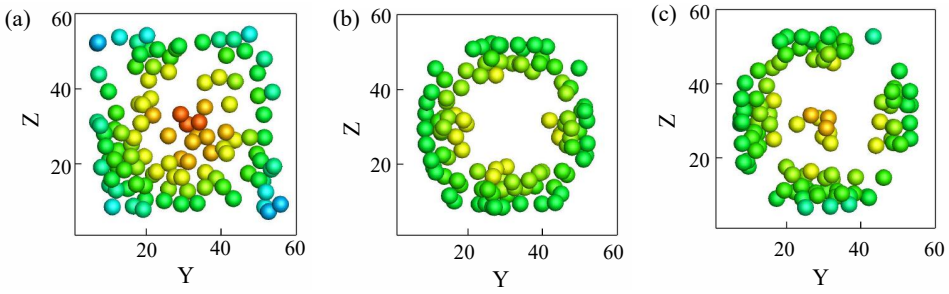

Fig. 7. Lateral distribution of non-adhesive particles under different pressure gradients: (a) Re = 6.75, (b) Re = 50 and (c) Re = 101.

which the agglomerate can keep stable. Thus, the stable distribution map in which two curves are obtained by connecting the limit points representing the upper and lower boundary can be obtained.

$$R_F = \frac{F_D}{F_C} = \frac{\mu d_p^s |\triangle U|}{\gamma r_e} \tag{27}$$

where d_p^s represents the diameter of smaller particle, m; $\triangle U$ represents the fluid flow velocity difference between the center of two particles, m/s; r_e represents the equivalent radius of two contacted particles, m.

In the stable aggregation distribution maps, the x-axis represents the distance between the agglomerate center and the central line of the channel, and the y-axis represents the distance between the member particle center and the central line of the channel (Fig. 9, Figs. S4-S5). If the y value falls between the upper and lower limits, this particle can stably adhere to the agglomerate. Otherwise, it will be torn apart by the hydrodynamic force. This map can help us analyze the size of agglomerate and their distribution. Fig. 9 presents the stable aggregation distribution map with varying surface energy values. When the surface energy is increased, the stable area becomes wider. Under a low surface energy, the stable area between the upper and lower limit lines for the agglomerate to keep intact has an elongated stripped shape, and it is difficult for particles to form large agglomerates under such a weak adhesive contacted force. Fig. S4 shows the map of changes in the stable aggregation distribution with the increase in Re. In this case, the stable area gradually narrows as a result of the stronger disturbance of hydrodynamic force. Fig. S5 portrays the stable aggregation distribution map for different particle concentrations; under the same Re and surface energy, they have the same shape.

In order to validate the above stable aggregation distribution map, the agglomerates are extracted from Fig. 8 and the results are shown in Fig. S6. For each extracted agglomerate, the distance between its center and the central line of the channel (position of the agglomerate) can be obtained. This distance is the corresponding x-value in the map, while the distance between every member particle of this agglomerate (the position of member particle) is the corresponding y-value. The center of the circumscribed box of the agglomerate is specified as its position (Fig. S7(a)). As for the position of member particle, Fig. S7(b) presents the search of the far end particles of the agglomerate, and P_f and P_n have the longest and the shortest distances away from the central line of the channel, respectively. The centers of most of the agglomerates are located at positions with a distance ranging from 12 to 18 away from the central line of the channel (2/10 to 3/10 of the characteristic dimension of the channel). The member particles in the agglomerates almost distribute in the stable area. A few upper far end particles in the agglomerate in case 9 are beyond the upper boundary. This means that the particle distribution does not reach a completely stable state and these particles beyond the boundary will be torn away from the agglomerate by hydrodynamic force.

4.2 Micro-particle migration in curved channel flow

For micro-particle migration in channels with a small characteristic dimension ratio, besides the interaction between particles, the effects of wall on the particle migration also play a key role. The geometric models of curved channels with different open angles (α) are built, where α reflects the magnitude of tortuosity and the initial distribution of micro-particles in them (Fig. S8). The channel apertures are the same and equal to 20 μm with a characteristic dimension ratio R_d of 4.0. The length along the flow direction and the width for

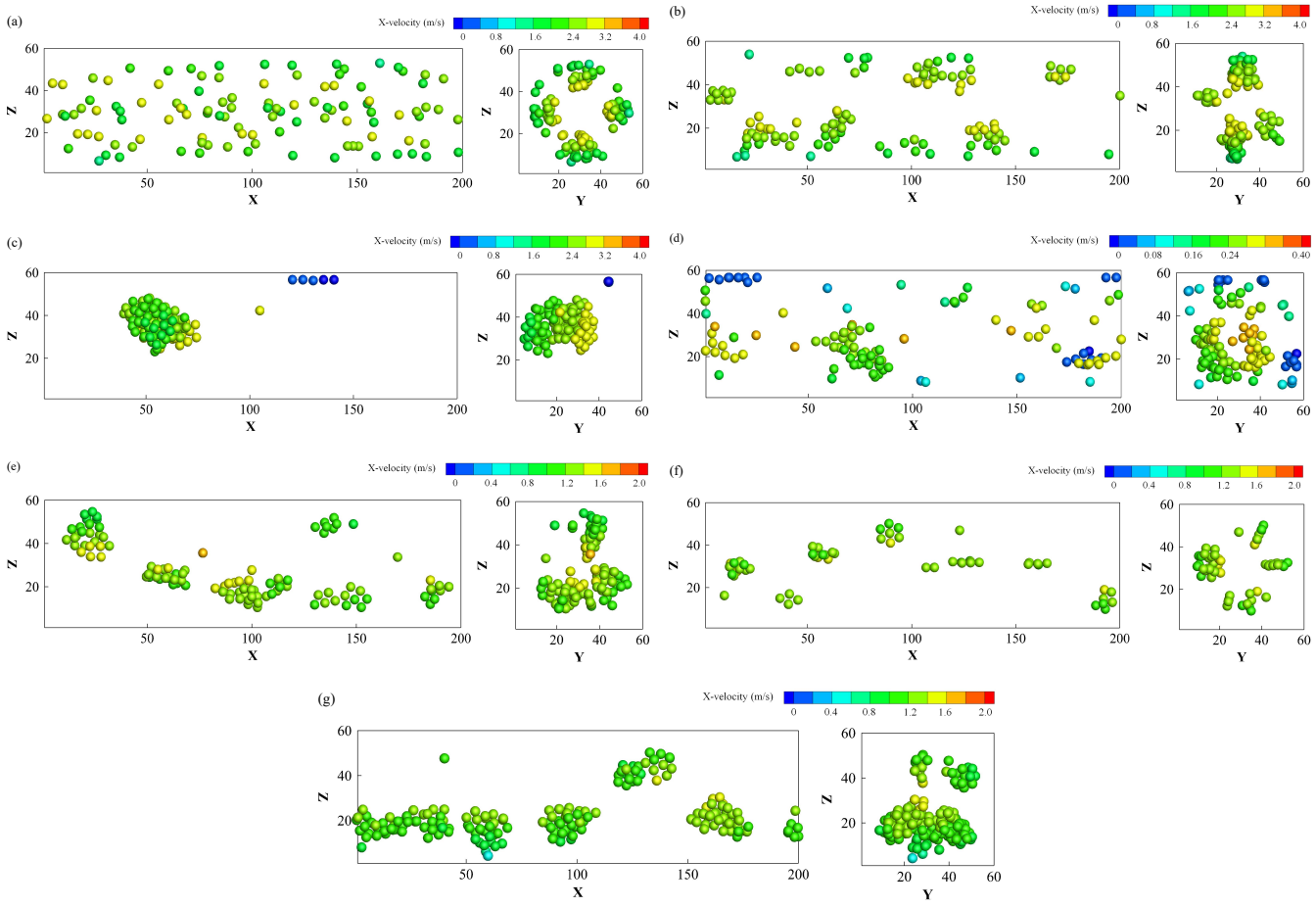

Fig. 8. Distribution of adhesive particles under different simulation parameters: (a) Re = 67.5, γ = 1 mJ/m^2, C_p = 1%; (b) Re = 67.5, γ = 3 mJ/m^2, C_p = 1%; (c) Re = 67.5, γ = 30 mJ/m^2, C_p = 1%; (d) Re = 6.75, γ = 3 mJ/m^2, C_p = 1%; (e) Re = 33.75, γ = 3 mJ/m^2, C_p = 1%; (f) Re = 33.75, γ = 3 mJ/m^2, C_p = 0.5% and (g) Re = 33.75, γ = 3 mJ/m^2, C_p = 1.5%.

Table 6. Simulation parameters for micro-particle migration in a curved channel.

Case	Open angle (°)	Pressure gradient (MPa/m)	Hydrodynamic and adhesive force ratio
1-2	60	3.19, 2.0	0.101, 0.064
3-4	90	2.7, 1.7	0.101, 0.064
5-6	120	2.33, 1.46	0.101, 0.064
7	180	2.0	0.101

these four geometric models are 130 and 30 μm, respectively. In the simulation, the surface energy for both particle and wall are set to be 3 mJ/m^2, and the particle concentration is 3%. Besides, the periodic boundary condition for fluid flow is used in both the x and the y directions, and the periodic boundary condition for the particle is applied only in the x direction. The boundary in the y direction is defined as the wall for particles without adhesive contact interaction with other particles.

The simulation parameters are listed in Table 6. For cases 1, 3, 5 and 7, the pressure gradients are set to make them exhibit the same average velocity magnitude of clean flow field. When the open angle is relatively small, such as $\alpha = 60°$ and $\alpha = 90°$, part of the flow space in Fig. 10 at the curved part has a relatively low velocity magnitude and the effective flow space is compressed. Smaller pressure gradients in cases 2, 4 and 6 are used to investigate the effects of hydrodynamic and adhesive force ratio on the migration and retention of particles.

During the migration of adhesive micro-particles in the channel, the collision between particles facilitates the formation of agglomerates. Besides the interaction between particles, for cases with small R_d, the effects of wall cannot be ignored. A video is useful to investigate the process of particle aggregation and retention. The link to the Videos of particle migration in curved channels from case 1 to case 7 can be found in the Supplementary material. While the particles near the wall are driven forward by the fluid flow, they will move towards the wall under the pushing action of other particles colliding with them and then will be captured by the wall, as shown in Fig. S9(a). The change of the velocity direction of particles at the curved part also increases the possibility of their collision with the wall. These captured particles stop on the surface of the wall or slowly move forward, and will further capture the following particles that collide with them. Therefore, the retention of single particles on the wall surface

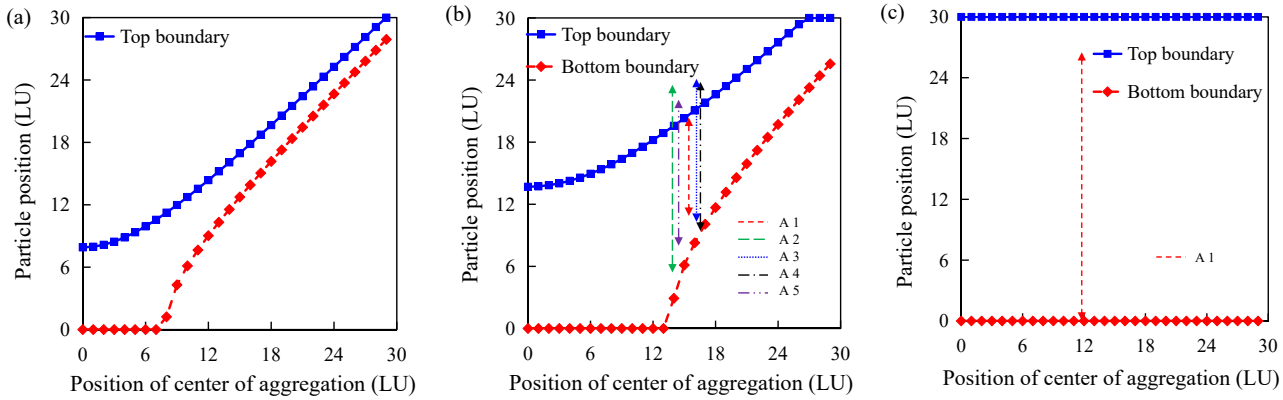

Fig. 9. Stable aggregation distribution map for different adhesive contacted forces: (a) γ = 1 mJ/m^2, (b) γ = 3 mJ/m^2 and (c) γ = 30 mJ/m^2.

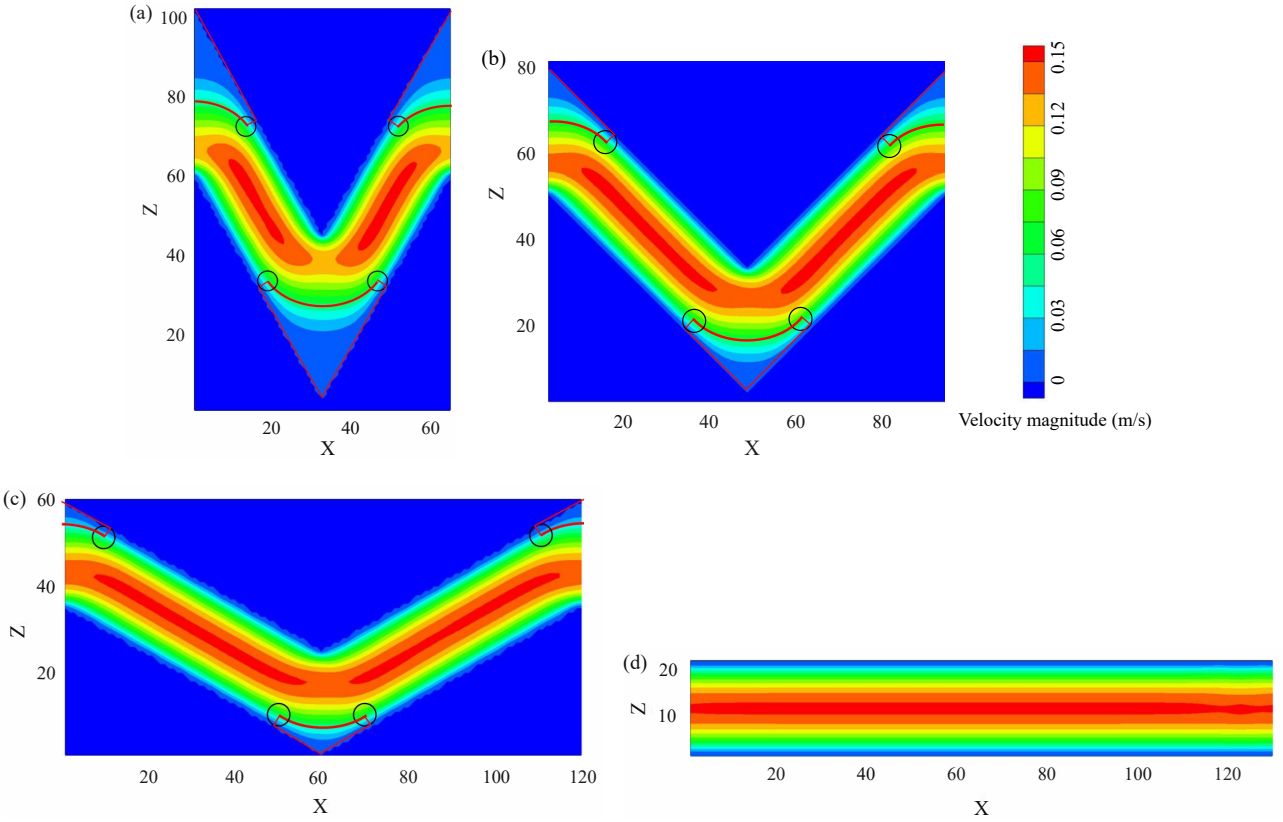

Fig. 10. The clean flow field: (a) α = 60°, (b) α = 90°, (c) α = 120° and (d) α = 180°.

is a significant factor to induce agglomerate formation. After a moving agglomerate collides with a captured one, resulting from the collision force and larger drag force, the newly formed larger agglomerate might detach from the wall and move in the channel again, as shown in Fig. S9(b). However, the newly formed large aggregation might also temporarily block the channel at the straight part or curved part, as shown in Figs. S9(c)-S9(d). The corresponding flow field slices depicted in Fig. S9 illustrate that the moving state of particles will have an obvious influence on the flow field, and the retention of particles can greatly decrease the conductivity of the channel.

The numerical results for all cases are concluded and a general particle migration process in a channel with small characteristic dimension ratio is obtained. The black-filled circle in Fig. 11 refers to the captured particle by the wall. The particle migration process includes single particle retention, capture of following particles, and migration of large agglomerate. If there are many particles contacting with the wall in a large agglomerate, the hydrodynamic force cannot overcome the adhesive force and will be blocked, as portrayed in Fig. 11(c). However, under the effects of drag force, the geometrical shape

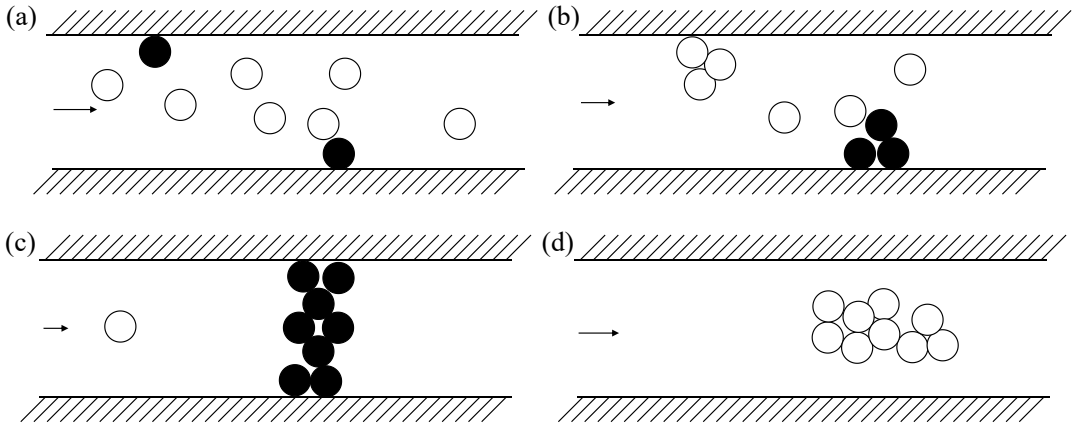

Fig. 11. Schematic diagram of the migration of adhesive particles in a channel with small characteristic dimension ratio: (a) Single particle retention, (b) capture of following particles, (c) large blocked aggregation and (d) large moving aggregation.

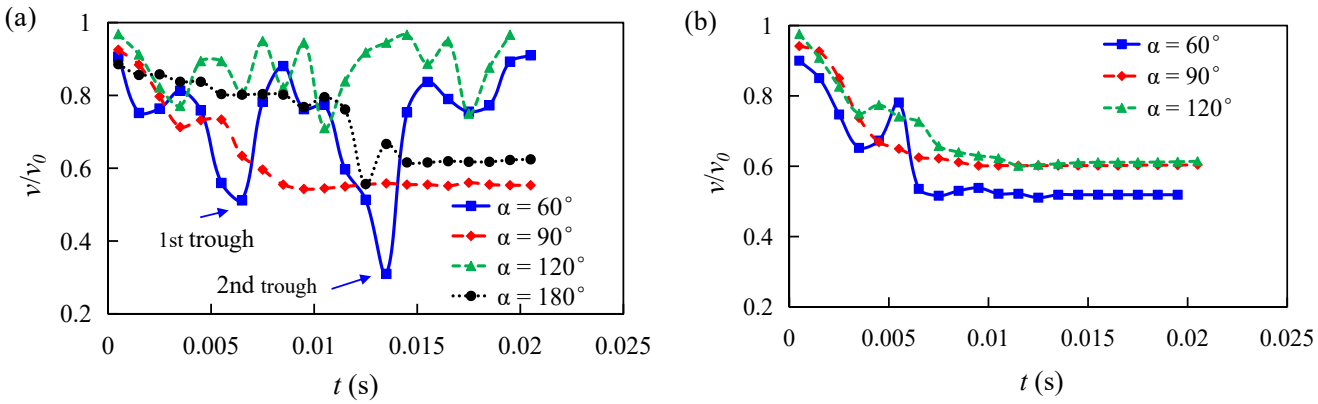

Fig. 12. Evolution of average velocity in channels: (a) R_F = 0.101 and (b) R_F = 0.064.

of the agglomerate and its contact conditions with the wall can gradually change, which may make it detach from the wall and move in the channel again, as shown in Fig. 11(d).

As described above, single particle retention is the factor promoting the formation of agglomerate. After analyzing the videos, the two factors accelerating the single particle retention in a curved channel are concluded. The first one is that the particles mainly distribute in the effective flow space that is compressed in the curved channel, and the high apparent particle concentration increases the particle collision frequency and promotes the particle movement towards the wall. The second factor is that some particles in the low velocity area of the channel that is enclosed by the red line in Fig. 10 are more likely to collide with the wall when they migrate in the flow and then stop or slowly move on the wall surface. The two factors above lead to the single particle retention in the curved channel occurring earlier and easier.

Under high R_F, the particles in channels with $\alpha = 90°$ and $\alpha = 180°$ are finally captured by the wall and the agglomerates are loose and dispersed, while particles in channels with $\alpha = 60°$ and $\alpha = 120°$ finally suspend in the fluid in the form of compact ellipsoidal agglomerate (Fig. S10(a)). Although the suspended ellipsoidal agglomerate in this study seems to have negligible effects on the fluid flow, in a real fracture system, the suspended large agglomerate is more likely to be blocked by a narrow channel during its migration and will greatly decrease the conductivity of the channel. After the R_F is decreased, as shown in Fig. S10(b), the particles in all channels are captured by the wall. Compared with that under high R_F, the captured agglomerates are looser and more dispersed. The high R_F means relatively larger drag force from the fluid flow and the particles cannot firmly stick to the wall. The temporarily captured particles are more likely to detach from the wall again. Therefore, under high R_F, the repeated capture and detachment of particles promote the formation of a large and compact agglomerate.

The evolution of dimensionless average velocity can reflect the variation in the conductivity of the channel (Fig. 12, in which the v_0 is the average velocity in the clean flow field). The initial v/v_0 decline rates in the curved channel are higher than those in a channel with $\alpha = 180°$, particularly in a channel with $\alpha = 60°$, where the average velocity decrease is the fastest and the largest. The curved channel can accelerate and improve the retention of particles on the wall. The repeated capture and detachment of agglomerate leads to the fluctuation of average velocity. The two troughs of average velocity in a

channel with $\alpha = 60^\circ$ in Fig. 12(a) correspond to the temporary blockage in Figs. S9(c)-S9(d), respectively. The two significant average velocity decreases are caused by blockage by large and compact agglomerate. The size and compaction degree of the captured agglomerate determines the falling range of average velocity. In a channel with $\alpha = 180^\circ$, although most particles are eventually captured by the wall, the agglomerates are relatively small and dispersed, and the average velocity has a lower deceasing rate than that in a channel with $\alpha = 90^\circ$.

In a channel with open angle = 90°, under low R_F, because the agglomerates are loose and dispersed, the final average velocity decrease rate is less than that under high R_F (Fig. 12(b)). Under the speculation that the suspended compact ellipsoidal agglomerates under high R_F shown in Fig. S10(a) are eventually captured by a narrow channel, the final average velocity decrease rate under low R_F will be generally less. In the experimental study on the fluid velocity sensitivity of coal by Tao et al. (2017), the permeability damage deteriorated with the increase in flow rate. Wei et al. (2019) experimentally studied the migration of fines in propped fracture, and the conductivity variation with the change in flow rate was not stable and monotonous. These experimental results can be explained by the above findings.

5. Conclusions

In this work, the LBM-DEM method coupled using the IMB scheme was introduced. Based on this method, particle-scale numerical simulations of micro-particle migration in duct flow in channels with large characteristic dimension ratio and with small characteristic dimension ratio were conducted. Based on the numerical results, the following conclusions can be drawn:

1) When the Re is increased, the enhanced lateral movement of particles facilitates the collision among them; however, a higher hydrodynamic force is unfavorable for the keeping of the formed agglomerate. The size of the agglomerate does not monotonously change with the increase in Re.
2) From the perspective of the balance between fluid force and adhesive force, a stable distribution map is proposed and validated. The center of the agglomerate generally locates at a lateral position away from the central line of the channel in a range of 2/10 to 3/10 of the characteristic dimension of the channel.
3) The particle migration process includes single particle retention, capture of following particles and migration of large agglomerate.
4) Single particle retention is a main factor promoting agglomerate formation. Two factors in the curved channel, namely, compressed effective flow space and the curved part, increase the collision between a particle that passes through it and the wall.
5) A higher fluid flow rate facilitates the formation of a large and compact agglomerate, and blockage by this can cause severe impairment of the conductivity of channel.

Acknowledgements

This work is financially supported by National Natural Science Foundation of China (No. 52004301).

Supplementary file

https://doi.org/10.46690/ager.2023.11.06

Conflict of interest

The authors declare no competing interest.

References

Abraham, F. F. Functional dependence of drag coefficient of a sphere on Reynolds number. The Physics of Fluids, 1970, 13(8): 2194-2195.

Bedrikovetsky, P., Siqueira, F. D., Furtado, C. A., et al. Modified particle detachment model for colloidal transport in porous media. Transport in Porous Media, 2011, 86(2): 353-383.

Berkowitz, N. An Introduction to Coal Technology. Amsterdam, Netherlands, Elsevier, 2012.

Bradford, S. A., Simunek, J., Bettahar, M., et al. Modeling colloid attachment, straining, and exclusion in saturated porous media. Environmental Science & Technology, 2003, 37: 2242-2250.

Chen, S., Li, S. Collision-induced breakage of agglomerates in homogenous isotropic turbulence laden with adhesive particles. Journal of Fluid Mechanics, 2020, 902: A28.

Chen, S., Li, S., Marshall, J. S. Exponential scaling in early-stage agglomeration of adhesive particles in turbulence. Physical Review Fluids, 2019, 4(2): 024304.

Chen, H., Liu, W., Chen, Z., et al. A numerical study on the sedimentation of adhesive particles in viscous fluids using LBM-LES-DEM. Powder Technology, 2021, 391: 467-478.

Choi, Y. S., Seo, K. W., Lee, S. J. Lateral and cross-lateral focusing of spherical particles in a square microchannel. Lab on a Chip, 2010, 11(3): 460-465.

Chun, B., Ladd, A. Inertial migration of neutrally buoyant particles in a square duct: An investigation of multiple equilibrium positions. Physics of Fluids, 2006, 18(3): 031704.

Close, J. C. Natural fractures in coal, in Hydrocarbons from Coal, edited by Law, B. E., and Rice, D. D., American Association of Petroleum Geologists, Tulsa, Oklahoma, pp. 119-132, 1993.

Cook, B. K. A numerical framework for the direct simulation of solid-fluid systems. Massachusetts Institute of Technology, 2001: 129-136.

Cook, B. K., Noble, D. R., Williams, J. R. A direct simulation method for particle-fluid systems. Engineering Computations, 2004, 21(2/3/4): 151-168.

Feng, J., Hu, H., Joseph, D. D. Direct simulation of initial value problems for the motion of solid bodies in a

Newtonian fluid. Part 2. Couette and Poiseuille flows. Journal of fluid Mechanics, 1994, 277: 271-301.

Feng, Z., Michaelides, E. E. The immersed boundary-lattice boltzmann method for solving fluid-particles interaction problem. Journal of Computational Physics, 2004, 195(2): 602-628.

Guo, Z., Zheng, C., Shi, B. Discrete lattice effects on the forcing term in the lattice Boltzmann method. Physical Review E, 2002, 65(4): 046308.

Hamaker, H. C. The London-van der Waals attraction between spherical particles. Physica, 1937, 4(10): 1058-1072.

Hertz, H. Über die Berührung fester elastische Körper. Journal Fur Die Reine Und Angewandte Mathematik, 1882, 92: 156-71. (in German)

Hu, S., Hao, Y., Chen, Y., et al. Dynamic influence law of coal powder migration and deposition on propped fracture permeability. Journal of China Coal Society, 2021, 46(4): 1288-1296. (in Chinese)

Johnson, K. L., Kendall, K., Roberts, A. Surface energy and the contact of elastic solids. Mathematical and Physical Sciences, 1971, 324(1558): 301-313.

Jones, B. D., Williams, J. R. Fast computation of accurate sphere-cube intersection volume. Engineering Computations, 2017, 34(4): 1204-1216.

Krüger, T. The Lattice Boltzmann Method: Principles and Practice. Berlin, Germany, Springer International Publishing, 2007.

Ladd, A. J. Numerical simulations of particulate suspensions via a discretized Boltzmann equation. Part 1. Theoretical foundation. Journal of Fluid Mechanics, 1994a, 271: 285-309.

Ladd, A. J. Numerical simulations of particulate suspensions via a discretized Boltzmann equation. Part 2. Numerical results. Journal of Fluid Mechanics, 1994b, 271: 311-339.

Liu, W., Wu, C. A hybrid LBM-DEM numerical approach with an improved immersed moving boundary method for complex particle-liquid flows involving adhesive particles. arXiv, 2019, 1901.09745.

Liu, W., Wu, C. Migration and agglomeration of adhesive microparticle suspensions in a pressure-driven duct flow. AIChE Journal, 2020, 66(6): e16974.

Marshall, J. S. Discrete-element modeling of particulate aerosol flows. Journal of Computational Physics, 2009, 228(5): 1541-1561.

McCullough, J. W. S., Aminossadati, S. M., Leonardi, C. R. Transport of particles suspended within a temperature-dependent viscosity fluid using coupled LBM-DEM. International Journal of Heat and Mass Transfer, 2020, 149: 119159.

McNamara, G. R., Zanetti, G. Use of the Boltzmann equation to simulate lattice-gas automata. Physical Review Letters, 1988, 61(20): 2332-2335.

Noble, D. R., Torczynski, J. R. A lattice-Boltzmann method for partially saturated computational cells. International Journal of Modern Physics C, 1998, 9(8): 1189-1201.

Norouzi, H. R., Zarghami, R., Sotudeh-Gharebagh, R., et al. Coupled CFD-DEM Modeling: Formulation, Implementation and Application to Multiphase Flows. Tehran, Iran, John Wiley & Sons, 2016.

Peskin, C. S. Flow patterns around heart valves: A digital computer method for solving the equations of motion. New York, Albert Einstein College of Medicine, Yeshiva University, 1972.

Qi, M., Li, Y., Moghanloo, R. G., et al. Applying deep bed filtration theory to study long-term impairment of fracture conductivity caused by reservoir fines. Geoenergy Science and Engineering, 2023, 231: 212253.

Qian, Y., d'Humières, D., Lallemand, P. Lattice BGK models for Navier-Stokes equation. EPL (Europhysics Letters), 1992, 17(6): 479-484.

Rousseau, D., Hadi, L., Nabzar, L. Injectivity decline from produced-water reinjection: New insights on in-depth particle-deposition mechanisms. SPE Production & Operations, 2008, 23: 525-531.

Shan, X., Chen, H. Lattice Boltzmann model for simulating flows with multiple phases and components. Physical Review E, 1993, 47(3): 1815-1819.

Shao, Y., Ruan, X., Li, S. Mechanism for clogging of microchannels by small particles with liquid cohesion. AIChE Journal, 2021, 67(7): e17288.

Strack, O. E., Cook, B. K. Three-dimensional immersed boundary conditions for moving solids in the lattice Boltzmann method. International Journal for Numerical Methods in Fluids, 2007, 55(2): 103-125.

Tao, S., Tang, D., Xu, H., et al. Fluid velocity sensitivity of coal reservoir and its effect on coalbed methane well productivity: A case of Baode Block, northeastern Ordos Basin, China. Journal of Petroleum Science and Engineering, 2017, 152: 229-237.

Tao, S., Zhang, H., Guo, Z., et al. A combined immersed boundary and discrete unified gas kinetic scheme for particle-fluid flows. Journal of Computational Physics, 2018, 375: 498-518.

Tsuji, Y., Kawaguchi, T., Tanaka, T. Discrete particle simulation of two-dimensional fluidized bed. Powder Technology, 1993, 77(1): 79-87.

Wang, M., Feng, Y., Owen, D. R. J., et al. A novel algorithm of immersed moving boundary scheme for fluid-particle interactions in DEM-LBM. Computer Methods in Applied Mechanics and Engineering, 2019, 346: 109-125.

Wang, M., Feng, Y., Pande, G. N., et al. A coupled 3-dimensional bonded discrete element and Lattice Boltzmann method for fluid-solid coupling in cohesive geomaterials. International Journal for Numerical and Analytical Methods in Geomechanics, 2018, 42(12): 1405-1424.

Wang, M., Feng, Y., Qu, T., et al. Instability and treatments of the coupled discrete element and lattice Boltzmann method by the immersed moving boundary scheme. International Journal for Numerical Methods in Engineering, 2020, 121(21): 4901-4919.

Wang, M., Feng, Y., Wang, C. Numerical investigation of initiation and propagation of hydraulic fracture using the coupled bonded particle-lattice Boltzmann method. Computers & Structures, 2017, 181: 32-40.

Wang, D., Wang, Z. 3D lattice Boltzmann method-discrete-element method with immersed moving boundary scheme

numerical modeling of microparticles migration carried by a fluid in fracture. SPE Journal, 2022, 27(5): 2841-2862.

Wang, D., Wang, Z., Cai, X. Experimental study on coal fines migration and effects on conductivity of hydraulic fracture during entire coalbed methane production period. Geoenergy Science and Engineering, 2023, 223: 211555.

Wei, Y., Li, C., Cao, D., et al. The effects of particle size and inorganic mineral content on fines migration in fracturing proppant during coalbed methane production. Journal of Petroleum Science and Engineering, 2019, 182: 106355.

Wolf-Gladrow, D. A. Lattice-gas Cellular Automata and Lattice Boltzmann Models: An Introduction. Berlin, Germany, Springer, 2004.

Wu, J. The coal surface energy calculation based on the adsorption method and its research significance. Coal Geology & Exploration, 1994, 22(2): 6. (in Chinese)

Wu, C., Guo, Y. Numerical modelling of suction filling using DEM/CFD. Chemical Engineering Science, 2012, 73: 231-238.

Yang, G., Jing, L., Kwok, C. Y., et al. A comprehensive parametric study of LBM-DEM for immersed granular flows. Computers and Geotechnics, 2019, 114: 103100.

Yang, G., Jing, L., Kwok, C. Y., et al. Pore-scale simulation of immersed granular collapse: Implications to submarine landslides. Journal of Geophysical Research: Earth Surface, 2020, 125(1): e2019JF005044.

Zamani, A., Maini, B. Flow of dispersed particles through porous media-deep bed filtration. Journal of Petroleum Science and Engineering, 2009, 69(1/2): 71-88.

Zhao, X., Liu, S., Sang, S., et al. Characteristics and generation mechanisms of coal fines in coalbed methane wells in the southern Qinshui Basin, China. Journal of Natural Gas Science & Engineering, 2016, 34: 849-863.

Zou, Y., Zhang, S., Zhang, J. Experimental method to simulate coal fines migration and coal fines aggregation prevention in the hydraulic fracture. Transport in Porous Media, 2014, 101: 17-34.